Journal of Materials Chemistry A

ROYAL SOCIETY OF CHEMISTRY

PAPER

View Article Online
View Journal

Cite this: DOI: 10.1039/d6ta00154h

Governing factors in mildly acidic Zn/MnO_2 batteries: interplay of electrochemical protocols, electrolyte composition, and cell configuration

Aldina Sultana, Alan Ferris, Colton King, Seongbak Moon and Veronica Augustyn *

Zn/MnO_2 aqueous batteries are promising candidates for long duration energy storage systems due to their use of cost-effective materials and inherent safety profile. In aqueous mildly acidic electrolytes, both electrodes ideally undergo reversible electrodeposition during charge and electrodissolution during discharge. Here, we report on the investigation of the electrodeposition and electrodissolution mechanisms of the MnO_2 cathode in mildly acidic Zn/MnO_2 batteries with different electrochemical protocols (galvanostatic or chronoamperometric) in both an aqueous and a hybrid aqueous-sulfolane electrolyte. *Ex situ* characterization with Raman spectroscopy and scanning electron microscopy revealed substantial heterogeneity in electrodeposited MnO_2 phases across both electrolyte systems. We used *operando* electrochemical optical spectroscopy (EC-OM) to further understand the electrochemical mechanisms including hydrogen evolution. We obtained the highest coulombic efficiency in a hybrid aqueous-sulfolane electrolyte, with short charging times of a few minutes using chronoamperometry, and a high surface area carbon scaffold. These parameters minimize the contribution from parasitic hydrogen evolution at the zinc anode and lead to the formation of dense but thin MnO_2 films that undergo the most efficient electrodissolution during discharge. Our results validate the beneficial properties of hybrid aqueous-sulfolane electrolytes and underscore the need to further stabilize the zinc anode and develop novel high surface area carbon scaffolds for efficient MnO_2 electrodeposition and electrodissolution for Zn/MnO_2 batteries operating in mildly acidic electrolytes.

Received 7th January 2026
Accepted 8th April 2026

DOI: 10.1039/d6ta00154h

rsc.li/materials-a

1. Introduction

The deployment of renewable energy conversion devices is fundamentally altering grid operations and driving a critical need for long-duration energy storage (LDES) technologies to ensure multi-hour system reliability.[1,2] LDES systems are engineered to provide sustained discharge ranging from several hours up to multiple days, enabling effective balancing during extended periods of renewable generation shortfalls. Commercially available LDES technologies exhibit energy capacity costs in the hundreds of US dollars per kilowatt-hour and/or utilize scarce materials, while advanced emerging technologies aim to achieve costs below $100 per kWh with sustainable and abundant elements to enable economically viable, large-scale grid deployment.[3,4] While lithium-ion batteries currently dominate grid storage installations, their inherent safety limitations such as flammability risks and thermal runaway hazards, coupled with geographical constraints on material supply chains,[5] motivate the search for new battery chemistries for LDES applications.[6,7] Rechargeable aqueous Zn/MnO_2 batteries present a safe and potentially low-cost option for LDES that leverages earth-abundant materials and non-flammable electrolytes.[8–10] The Zn anode has a high theoretical capacity of 820 mA h g^{-1}, while the MnO_2 cathode offers a theoretical capacity of 616 mA h g^{-1} based on a 2 electron redox mechanism. Under mildly acidic conditions, these batteries operate *via* reversible electrodeposition (during charge) and electrodissolution (during discharge)[11–14] reactions at both electrodes:

$$\text{Anode: } Zn_{(aq)}^{2+} + 2e^- \rightleftharpoons Zn_{(s)} \quad (1)$$

$$\text{Cathode: } Mn_{(aq)}^{2+} + 2H_2O_{(l)} \rightleftharpoons MnO_{2(s)} + 4H_{(aq)}^{+} + 2e^- \quad (2)$$

An anode and cathode-free battery configuration offers distinct advantages by lowering active-material costs and eliminating conventional electrode preparation steps.[15,16] In this configuration, cells are assembled with only the electrode "current collectors" on both the positive and negative sides, and the active materials electrodeposit during initial charging. The cycling can be performed using different electrochemical protocols, most prominently using constant current (galvanostatic) or constant potential (chronoamperometric) methods.[11,13] In these conversion reactions, controlling the morphology, uniformity, and structural integrity of the electrodeposited materials remains a key challenge, as is

Department of Materials Science and Engineering, North Carolina State University, Raleigh, NC 27695, USA. E-mail: vaugust@ncsu.edu

suppressing dendritic or porous Zn electrodeposits and parasitic water decomposition reactions.

Electrodeposited MnO_2 typically comprises a mixture of disordered gamma (γ) MnO_2, an intergrowth structure containing domains of rutile β-MnO_2 and ramsdellite R-MnO_2 as well as hexagonal ε-MnO_2.[13,17] The phase distribution of the intergrowth phase and its microstructure strongly depend on the electrochemical charge protocol.[18,19] The efficiency of the battery is dependent on the morphology and thickness of MnO_2 formed during charging. In mildly acidic electrolytes, Zn electrodeposition on the anode competes with the hydrogen evolution reaction (HER), a parasitic proton-coupled electron transfer (PCET) reaction that lowers the coulombic efficiency, cycling stability, and calendar life.[20,21] While applying high currents or large potentials can minimize HER during zinc electrodeposition, hydrogen evolution also takes place at open circuit conditions due to the inherently low potential of zinc *vs.* RHE (−0.7 V). This leads to zinc corrosion and poor calendar life. Many approaches have been developed to suppress the HER and improve the reversibility of Zn electrodeposition/electrodissolution and calendar life.[22–26] Among these, hybrid electrolytes, formulated by combining aqueous and nonaqueous solvents, have shown promising performance.[27–33] A previous study reported a hybrid aqueous electrolyte for "anode-free" and "cathode-free" Zn/MnO_2 batteries consisting of 1 M $Zn(OTf)_2$ + 0.5 M $MnCl_2$ in 70 wt% sulfolane + 30 wt% water that showed long cycling stability, attributed to suppression of the HER at the anode and the oxygen evolution reaction (OER) at the cathode.[30] An open question in the field of hybrid electrolytes is the role of electrochemical cycling protocols on the observed behavior.

Here, we investigated the electrodeposition and electrodissolution mechanisms of MnO_2 in an initially "cathode-free" and "anode-free" Zn/MnO_2 battery using different electrochemical protocols in both mildly acidic aqueous and hybrid aqueous-sulfolane electrolytes. We combined *ex situ* Raman spectroscopy, scanning electron microscopy (SEM), and *operando* electrochemical optical microscopy (EC-OM) to quantify how the electrochemical protocol, cell configuration, and electrolyte environment influenced MnO_2 morphology and utilization. We observed a direct correlation between the deposition thickness and structural heterogeneity of MnO_2 films. Furthermore, we identified that the MnO_2 utilization upon discharge (MnO_2 electrodissolution) is primarily limited by two factors: (i) imbalance of the capacity at the zinc anode due to the parasitic HER, and (ii) kinetic barriers associated with thicker MnO_2 deposits at the cathode. These can be overcome through fast charging protocols that minimize parasitic HER and the use of high surface area carbon scaffolds at the cathode that facilitate thin MnO_2 deposits while allowing for high areal capacities.

2. Experimental methods

2.1 Chemicals

All chemicals were used as received. Zinc sulfate heptahydrate ($ZnSO_4 \cdot 7H_2O$; 99%; ACS reagent), manganese(II) sulfate tetrahydrate ($MnSO_4 \cdot 4H_2O$; 99%), zinc trifluoromethanesulfonate ($C_2F_6O_6S_2Zn$; 98%), manganese chloride tetrahydrate ($MnCl_4 \cdot 4H_2O$; Crystalline/Certified ACS), sulfolane ($(CH_2)_4SO_2$; 99%) were purchased from Fisher Scientific. Copper foil (9 μm thick) was purchased from MTI Corp. Graphite foil (Ceramaterials) was obtained from the research group of William Chueh at Stanford University. Soft graphite felt was purchased from Ali Express. The PFA Swagelok tube fitting (Union; 1/2 in) was purchased from Swagelok. Titanium rod current collector (12.7 mm diameter; annealed; 99.5% (metals basis)), Cytiva Whatman™ Binder-Free Glass Microfiber Prefiters (Grade GF/D; 125 mm diameter) were purchased from Fisher Scientific.

2.2 Electrochemical characterization

Electrochemical characterization was performed with a potentiostat (Bio-Logic MPG-2). The three-electrode cell (Fig. S1a) was assembled in a 50 mL three-neck round-bottom glass flask with graphite foil as the working electrode, an Ag/AgCl reference electrode, and Cu foil as the counter electrode. The electrolyte was 15 mL of an aqueous solution containing 1 M $MnSO_4$ and 1 M $ZnSO_4$ (pH ≈ 3.3). Electrolyte pH was measured with a pH meter (Mettler-Toledo Five Easy Benchtop F20). Galvanostatic charge–discharge (GCD) experiments were performed at ±0.05 mA cm^{-2} within a −0.2 V to 0.85 V potential window (*vs.* Ag/AgCl). The Zn/MnO_2 two-electrode cell (Fig. S1b) was assembled in a 50 mL three-neck flask with graphite foil as the cathode and copper foil as the anode, using 15 mL of electrolyte. The electrolytes used were 1 M $MnSO_4$ + 1 M $ZnSO_4$ in deionized (DI) water (aqueous) (pH ≈ 3.3) and 1 m $Zn(OTf)_2$ + 0.5 m $MnCl_2$ in 70 wt% sulfolane and 30 wt% water (hybrid) (pH ≈ 2.7). The electrode area exposed to the electrolyte was 2.0 cm^2. GCD experiments were performed at ±0.05 mA cm^{-2} within a 0.75 V to 1.85 V window. Time-dependent GCD experiments were performed at ±0.05 mA cm^{-2} for 3, 5, and 10 h between 0.75 V and 2.0 V. Chronoamperometry (CA) experiments were performed at a constant potential of 2.3 V until areal capacities of 0.01, 0.17, and 0.50 mA h cm^{-2} were reached, followed by discharge at a constant current density to a 1.0 V cut-off. The Zn/MnO_2 Swagelok cell (Fig. S1c) consisted of a 9 mm-diameter graphite felt cathode and a 9 mm diameter Cu foil anode, separated by a 10 mm-diameter glass microfiber separator soaked with 500 μL of the aqueous or hybrid electrolyte. CA charge took place at 2.3 V to obtain areal capacities of 0.5, 1, 2, and 5 mA h cm^{-2}, followed by galvanostatic discharge to 1.0 V. To obtain electrochemical surface area (ECSA) of the graphite felt, we performed cyclic voltammetry (CV; Fig. S2) of the porous graphite felt in a three-electrode Swagelok T-cell using activated carbon as the counter electrode and Ag/AgCl in saturated KCl as the reference electrode. A 1 M Na_2SO_4 solution (pH 6.8) was used as the electrolyte. The measurements were carried out at 20 mV s^{-1} between 0 V and 0.6 V for 250 cycles. The ECSA was calculated from the anodic current obtained in the 250th cycle (see SI for more details).

2.3 Physical characterization

Raman spectroscopy was conducted using a confocal Raman microscope (Witec Alpha 300) equipped with a 532 nm Nd:YAG laser, a 600 grooves per cm grating (spectral resolution

$\sim$3 cm^{-1}), and a 63$\times$ Zeiss water dipping objective lens (Fig. S3). The laser wavelength was calibrated to the main peak of Si at 520 cm^{-1}. Data analysis was performed with Python to subtract the background and generate a spline plot. The electrode microstructure was characterized using a high-resolution scanning electron microscope (SEM; Field Emission FEI Verios 460L or Hitachi SU8700). Images were acquired at accelerating voltages of 2 and 5 keV using a secondary electron detector at a working distance of $\sim$3 to 5 mm. Samples were mounted on conductive carbon tape, and multiple regions were scanned at different magnifications to ensure representative analysis. Roughness was determined using a confocal laser scanning microscope (Keyence VKx1100). The corresponding laser optical microscopy images of electrodeposited MnO_2 are shown in Fig. S4. The analysis was performed according to JIS B0601:2001(ISO 4287:1997) using identical filtering conditions for all samples (λ_s = 0.25 μm, λ_c = 0.25 mm). Values were extracted from the same surface analysis procedure for both samples to enable direct comparison and are shown in Table S1.

2.4 *Operando* electrochemical optical microscopy (EC-OM)

Operando observation of the electrodeposition and electrodissolution of the Zn/MnO_2 cell was performed using a 4K digital microscope (Dino-Lite EdgePLUS AM8917MZTL; resolution: 3840 $\times$ 2160, magnification: 10–140$\times$). The experimental setup is shown in Fig. S5. A 3.5 mL cuvette (PerkinElmer US LLC Special Quartz Macro Cuvette) was used as the electrochemical cell, with graphite foil and Cu foil electrodes affixed to the inner side wall of the cuvette using double-sided tape, providing a planar view of the 0.17 cm $\times$ 0.2 cm electrode area. For each video acquisition, the optical microscope was set to 120$\times$ magnification with a shutter speed of 1/11 s. Brightness was adjusted to 158 with a contrast setting of 40. Image acquisition was synchronized with electrochemical measurements collected using a potentiostat (BioLogic SP300). During GCD cycling at $\pm$0.05 mA cm^{-2}, frames were captured every 30 s and compiled into a 30 fps time-lapse video. For MnO_2 electrodeposition at 0.05 mA cm^{-2}, the video recording was paused for 30 s intervals while the microscope light brightness was increased to improve image resolution. During chronoamperometric deposition at 2.3 V to a specific capacity of 0.5 mA h cm^{-2} followed by galvanostatic discharge at a constant current density of 5 mA cm^{-2} to a cutoff potential of 0.75 V, video was recorded continuously in real time without time-lapse compression. For both experimental conditions, MnO_2 and Zn electrodeposition/electrodissolution processes were recorded in separate experimental runs under identical electrochemical conditions and cell configurations. Electrochemical datasets and videos were synchronized and merged into a single movie file using a custom Python script. Speed factors of the videos are shown in Table S2.

3. Results and discussion

3.1 Electrochemical characterization of the Zn/MnO_2 cell

We performed galvanostatic charge–discharge (GCD) at $\pm$0.05 mA cm^{-2} to evaluate Zn/MnO_2 utilization in a three or two electrode cell configuration (Fig. 1). All tests started with no MnO_2 on the graphite foil electrode and no Zn on the Cu foil electrode and immersed in an aqueous electrolyte (1 M $ZnSO_4$ + 1 M $MnSO_4$). In the three-electrode configuration (Fig. 1a and c), application of an anodic current leads to MnO_2 electrodeposition on the working electrode at a potential of 0.82 V *vs.* Ag/AgCl. Electrodissolution of MnO_2 takes place between 0.82 V and $-$0.2 V *vs.* Ag/AgCl upon the application of a cathodic current. In this configuration, we observed 88% coulombic efficiency (CE). Since the three-electrode cell isolates MnO_2 electrodeposition/electrodissolution at the graphite foil working electrode from electrochemical reactions at the counter electrode, this % CE directly reflects the ability to electrodissolve MnO_2 (Fig. 1c). We hypothesize that the 12% loss stems from kinetic limitations related to the electrodissolution of thicker, electronically insulated MnO_2 electrodeposits formed on the graphite foil (*vide infra*). We also note that the voltage profile in the three-electrode configuration displays distinct plateaus at 0.3 V and 0 V, which are absent in the two-electrode configuration. We attribute these plateaus to the precipitation of $Zn_4SO_4(OH)_6\cdot 5H_2O$ (ZHS) which occurs due to the increase in the interfacial pH as MnO_2 electrodissolution requires proton-coupled electron transfer (eqn (2)).[13,34,35]

In the two-electrode configuration (Fig. 1b and d), ideally during charge, soluble Mn^{2+} is oxidized at the cathode to form electrodeposited solid MnO_2 and Zn^{2+} is reduced at the anode to plate Zn metal. During discharge, MnO_2 is ideally reduced to soluble Mn^{2+} and the Zn is oxidized to soluble Zn^{2+}. In the two-electrode Zn/MnO_2 cell configuration, we observed 12% CE, a large decrease from the three-electrode configuration. In the two-electrode cell, this % CE reflects the combined reversibility of electrochemical processes taking place at the cathode and anode (Fig. 1d). At the anode (Cu foil), the HER competes with Zn electrodeposition during charge. In the aqueous electrolyte during galvanostatic charging, we predict that a significant fraction of the charge at the anode goes towards the HER, resulting in less Zn plating and, consequently, limited inventory of Zn to electrodissolve on discharge. At the cathode, MnO_2 electrodeposited during charge forms a relatively thick layer, and within the imposed discharge window and given the lower Zn inventory, kinetic transport limitations prevent complete MnO_2 electrodissolution. Therefore, MnO_2 will continue to accumulate with each cycle, leading to decreased % CE over time. To test our theory, we replaced the Cu foil electrode with Zn foil, resulting in a Zn foil‖graphite foil configuration (Fig. S6). Replacing Cu with Zn foil increased the Zn inventory of the two-electrode Zn–MnO_2 aqueous battery, increasing the % CE of the cell to $\sim$40%. The electrolyte composition has been shown to play a prominent role in suppressing the HER during Zn electrodeposition.[27,29] To investigate this effect here, we utilized a previously reported sulfolane-aqueous hybrid electrolyte for Zn–MnO_2 batteries.[30] In the Zn foil‖graphite foil configuration with the hybrid electrolyte, the two-electrode system reached 95% CE, consistent with prior reports that hybrid electrolytes effectively suppress the HER during Zn electrodeposition, increasing the Zn inventory available during discharge, and allowing for more complete electrodissolution of the MnO_2 at the cathode.

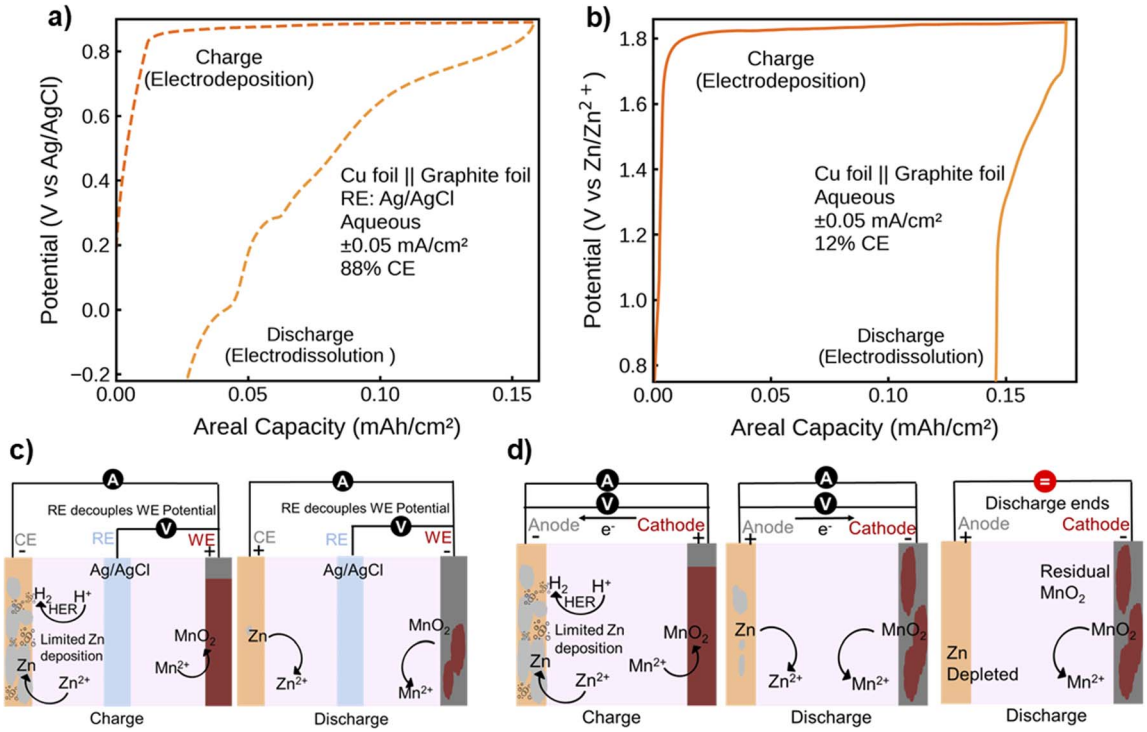

Fig. 1 Electrochemical cell configuration affects coulombic efficiency. The three-electrode cell (a) isolates cathodic MnO_2 electrodeposition, resulting in high CE (88%), whereas the two-electrode configuration (b) shows substantially reduced CE (12%), primarily limited by lower Zn inventory due to the competing hydrogen evolution. Schematic illustration of Zn/MnO_2 charge–discharge processes in a (c) three-electrode configuration and (d) two-electrode configuration. All experiments were performed in aqueous electrolyte (1 M $ZnSO_4$ + 1 M $MnSO_4$).

3.2 Influence of electrochemical parameters on the electrodeposition/electrodissolution of MnO_2

The Zn–MnO_2 battery literature reports the use of galvanostatic and potentiostatic charging and discharging protocols. To understand the influence of these parameters on the microstructure of the electrodeposited phases and their subsequent electrodissolution, we investigated MnO_2 electrodeposition under galvanostatic cycling by cycling two-electrode (Cu foil‖graphite foil) cells at a current density of ±0.05 mA cm^{-2} within a 0.75 to 2.0 V window in aqueous and hybrid electrolytes (Fig. 2a–c & Fig. S7). Charge durations of 3, 5, and 10 hours at this rate provide areal capacities of ∼0.155, 0.25, and 0.50 mA h cm^{-2}, respectively. In the hybrid electrolyte, the charge profiles were steeper and consistently reached the 2.0 V cut-off. We hypothesize that this occurs because of less HER at the zinc anode in the hybrid electrolyte. Consequently, the discharge capacity in the hybrid electrolyte exceeded that observed in the aqueous electrolyte. We observed that coulombic efficiency increased from 3 hours to 5 hours, reaching 40% in the aqueous system and 58.3% in the hybrid system, compared with 26% and 42% at 3 hours, respectively. However, at 10 hours, the coulombic efficiency decreased to 30% for the aqueous system and 40% for the hybrid system. We attributed the drop at 10 hours to kinetic limitations associated with the electrodissolution of thicker MnO_2 films, which restrict complete electrodissolution within the potential window.

We performed *ex situ* Raman spectroscopy to characterize electrodeposited MnO_2 formed in aqueous and hybrid electrolytes (Fig. 2d). The Raman spectra exhibited peaks in three regions associated with MnO_2: (1) ∼504–509 cm^{-1} (Mn–O–Mn bending), (2) 565–573 cm^{-1} (Mn–O stretching of edge-sharing MnO_6 units), and (3) 644–674 cm^{-1} (symmetric Mn–O stretching of MnO_6 octahedra). These features are characteristic of electrolytic MnO_2, an intergrowth phase composed of gamma (γ) and epsilon (ε) MnO_2. Prior literature reports that both polymorphs are defect-rich.[36–38] In γ-MnO_2, the dominant defects are structural intergrowths of pyrolusite blocks within a ramsdellite matrix (De Wolff defects), together with crystallographic twinning, both of which perturb the local MnO_6 connectivity and shift the Raman-active stretching modes. In ε-MnO_2, defect populations include Mn-sublattice vacancies and anti-phase domain boundaries, which generate local strain, disrupt long-range ordering, and broaden the distribution of Mn–O bond environments. Accordingly, Raman peak positions in the 500–700 cm^{-1} region vary with defect density and local lattice distortion. Consistent with these reports, we observed spatial variations in peak position and intensity, most prominently in the high-wavenumber region (640–690 cm^{-1}). In the aqueous electrolyte, this band appeared at 644–653 cm^{-1}, whereas in the hybrid electrolyte it shifted to 664–674 cm^{-1}. For each electrode, we collected spectra at ten spots and computed the standard deviation relative to the modal spectrum; the shaded area in Fig. 2d quantifies this variability. We define the

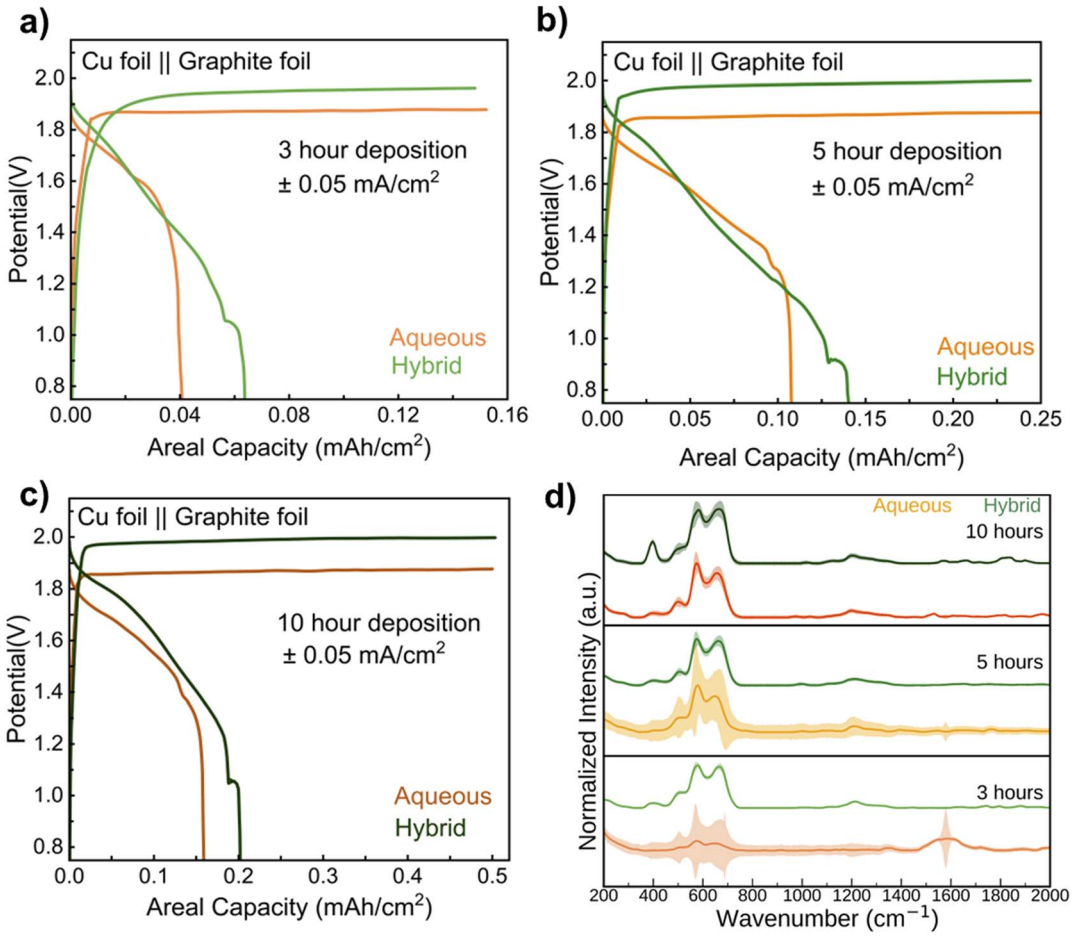

Fig. 2 Electrolyte and charge duration govern MnO_2 electrodeposition density, utilization, and structural homogeneity. Galvanostatic charge–discharge profiles of Cu foil||graphite foil cells in aqueous (orange) and hybrid (green) electrolytes, recorded at 0.05 mA cm^{-2} within a 0.75 to 2.0 V window for charge–discharge durations of (a) 3 hours, (b) 5 hours, and (c) 10 hours. (d) *Ex situ* Raman spectra of electrodeposited MnO_2 on graphite foil from aqueous and hybrid electrolytes show time-dependent structural evolution. The shaded regions represent structural heterogeneity, which decreased with longer deposition times, indicating increased homogeneity.

shaded area as the degree of structural heterogeneity of each electrodeposited sample. After 3 and 5 hours of deposition, the MnO_2 coatings formed in the aqueous electrolyte exhibited significantly greater heterogeneity than those deposited in the hybrid electrolyte. Raman spectra collected after 3 hours of deposition exhibit a strong peak at 1593 cm^{-1}, corresponding to the exposed graphite foil substrate (Fig. S8). After 5 hours of deposition, the presence of a shaded area around 1593 cm^{-1} indicates incomplete MnO_2 coverage. It suggests that some regions of the graphite foil remain uncovered even at this stage and electrodeposited MnO_2 does not form a continuous, uniform layer over the graphite substrate. The heterogeneity decreased after 10 h of electrodeposition, indicating that thicker deposits are structurally homogeneous in both aqueous and hybrid electrolyte systems.

To further investigate the morphological growth of electrodeposited MnO_2 as a function of deposition time and electrolyte composition, we performed SEM on electrodeposited MnO_2 after 3, 5, and 10 hours of galvanostatic charging in both electrolytes (Fig. 3). Plan-view SEM (Fig. 3a and c) reveals a time-dependent progression: discrete spheroidal aggregates at 3 hours, partially coalesced domains with increased areal coverage at 5 hours, and a continuous MnO_2 film by 10 hours in both electrolytes. At 3 and 5 hours, the hybrid electrolyte produced smaller particles with a narrower size distribution, while the aqueous electrolyte resulted in larger particles and notable surface heterogeneity. In the aqueous electrolyte, morphological uniformity only appeared after 10 hours of charging. These morphological trends align with our Raman spectroscopy results, which show decreasing spectral heterogeneity as deposition time increases. Cross-sectional SEM (Fig. 3b and d) confirms continuous MnO_2 layers on graphite foil with thicknesses of ~2.53 μm (aqueous) and ~2.24 μm (hybrid) at 10 h. However, both samples show deviation in MnO_2 layer thickness across the cross-section, indicating nonuniform growth on the graphite foil (Table S3).

We also investigated a fast charge–discharge protocol to assess its influence on MnO_2 electrodeposition. A constant potential of 2.3 V (chronoamperometry) was applied until areal capacities of 0.01, 0.17, and 0.50 mA h cm^{-2} were reached,

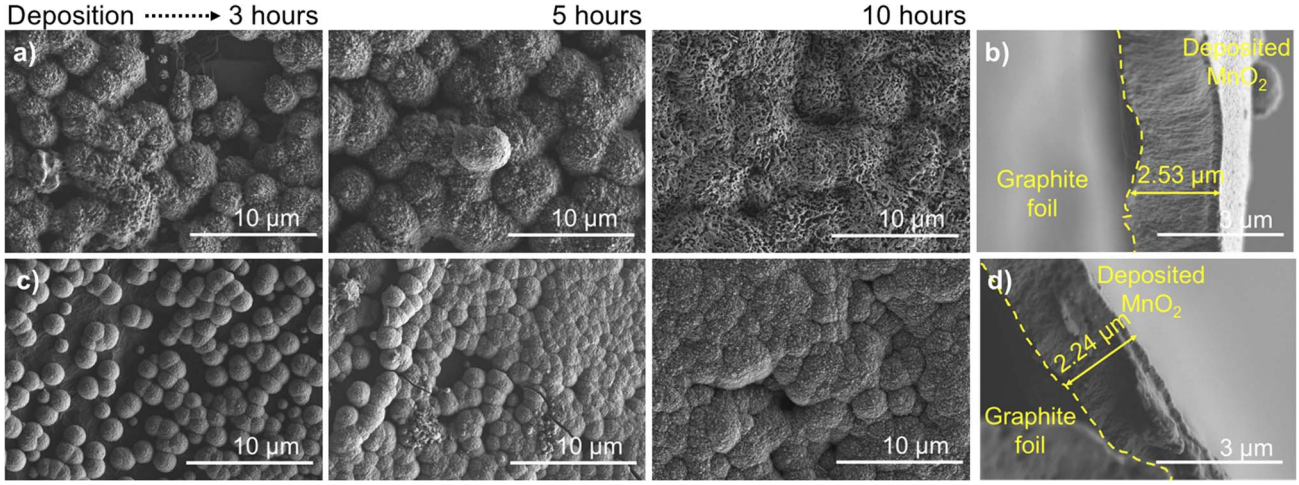

Fig. 3 Electrodeposition time and electrolyte composition dictate MnO_2 morphology and thickness during galvanostatic deposition at 0.05 mA cm^{-2}. SEM images of deposited MnO_2 at different deposition times in (a) aqueous electrolyte and (c) hybrid electrolyte. Cross-sectional SEM after 10 hours shows MnO_2 layer thickness of ~2.5 μm in (b) aqueous and ~2.2 μm in (d) hybrid electrolytes.

followed by discharge at constant current densities of 0.1, 1.7, and 5 mA cm^{-2}, respectively (Fig. 4a–c). Applying 2.3 V leads to high instantaneous currents over a short period of time (within minutes; Fig. S9), which results in the rapid deposition of dense MnO_2 and Zn films (*vide infra*) onto the graphite and Cu foil electrodes, respectively. Electrochemical cycling demonstrates an inverse relationship between % CE and areal capacity, revealing kinetic and transport limitations. Thicker, denser MnO_2 deposits formed during charge at higher capacities do not fully dissolve during discharge, suggesting incomplete electrodissolution consistent with the behavior observed under slow GCD protocols. For a given areal capacity, the aqueous electrolyte yielded higher discharge capacity than the hybrid electrolyte. We attribute this to the hybrid electrolyte's suppression of parasitic reactions, which directs more charge into MnO_2 deposition and produces denser, less accessible films that resist dissolution. In contrast, the aqueous system undergoes OER[30] at 2.3 V, which diverts charge but results in thinner, more porous MnO_2 deposits that dissolve more readily during high-rate discharge. However, during extended cycling, the hybrid electrolyte outperforms the aqueous system in efficiency (Fig. S10). We attribute the poor long-term performance of the aqueous electrolyte to the cumulative effects of parasitic oxygen evolution and hydrogen evolution reactions, which progressively consume water and alter the electrolyte concentration and pH.

In the fast-charging protocol (total charge time ≈ 5–10 min), the brief deposition period contrasts sharply with the prolonged galvanostatic deposition, where HER is more pronounced. A previous study[39] suggested that water in the zinc hexaaquo complex, $[Zn(H_2O)_6]^{2+}$, plays a key role in promoting the HER. During slow charging, the interfacial concentration of $[Zn(H_2O)_6]^{2+}$ remains relatively high. In contrast, during fast charge, a steeper interfacial concentration gradient forms, leading to a lower abundance of $[Zn(H_2O)_6]^{2+}$ that mitigates hydrogen evolution.[39] Another study directly compared hydrogen evolution during Zn deposition at different current densities and showed that interfacial pH gradients govern this behavior.[40] At high current densities, steep pH gradients rapidly promote the formation of a dense, uniform SEI or passivation layer, which suppresses HER and improves coulombic efficiency. By contrast, at low current density, weaker pH gradients delay formation of the protective interphase, allowing HER to persist for longer. On the other hand, during fast discharge, rapid proton consumption at the MnO_2 cathode raises the local pH and establishes a steep interfacial-to-bulk pH gradient, which slows MnO_2 dissolution because it proceeds *via* a proton-coupled electron transfer (PCET) mechanism. The elevated interfacial pH also promotes ZHS precipitation, partially passivating the cathode surface and introducing an additional diffusion barrier to charge transfer and mass transport.[41,42]

To gain deeper mechanistic insight, we employed fast CA charging to a specific capacity of 0.25 mA h cm^{-2} followed by slow galvanostatic discharge at 0.05 mA cm^{-2} (Fig. S12). Additionally, we incorporated a rest period of approximately 4.8 hours between the fast charge and slow discharge steps (Fig. S11a). We observed drastic differences in the discharge profiles for the aqueous electrolyte between these two protocols. Without any rest period, the coulombic efficiency reached 64%, whereas after the 4.8 h rest period, the coulombic efficiency dropped to 25% during discharge at 0.05 mA cm^{-2}. This substantial capacity loss supports the hypothesis of Zn corrosion during the rest period. The reduced availability of plated Zn directly translates to lower discharge capacity. Additionally, the plateau associated with ZHS precipitation shifted from ~1.3 V to 1.5 V, which is consistent with hydrogen evolution at open circuit leading to increased interfacial pH and earlier onset of ZHS formation. In contrast, for the hybrid electrolyte, no plateau associated with ZHS formation is observed in discharge profile, and the discharge capacity remains nearly identical for both protocols. This result demonstrates that the hybrid electrolyte effectively suppresses both chemical

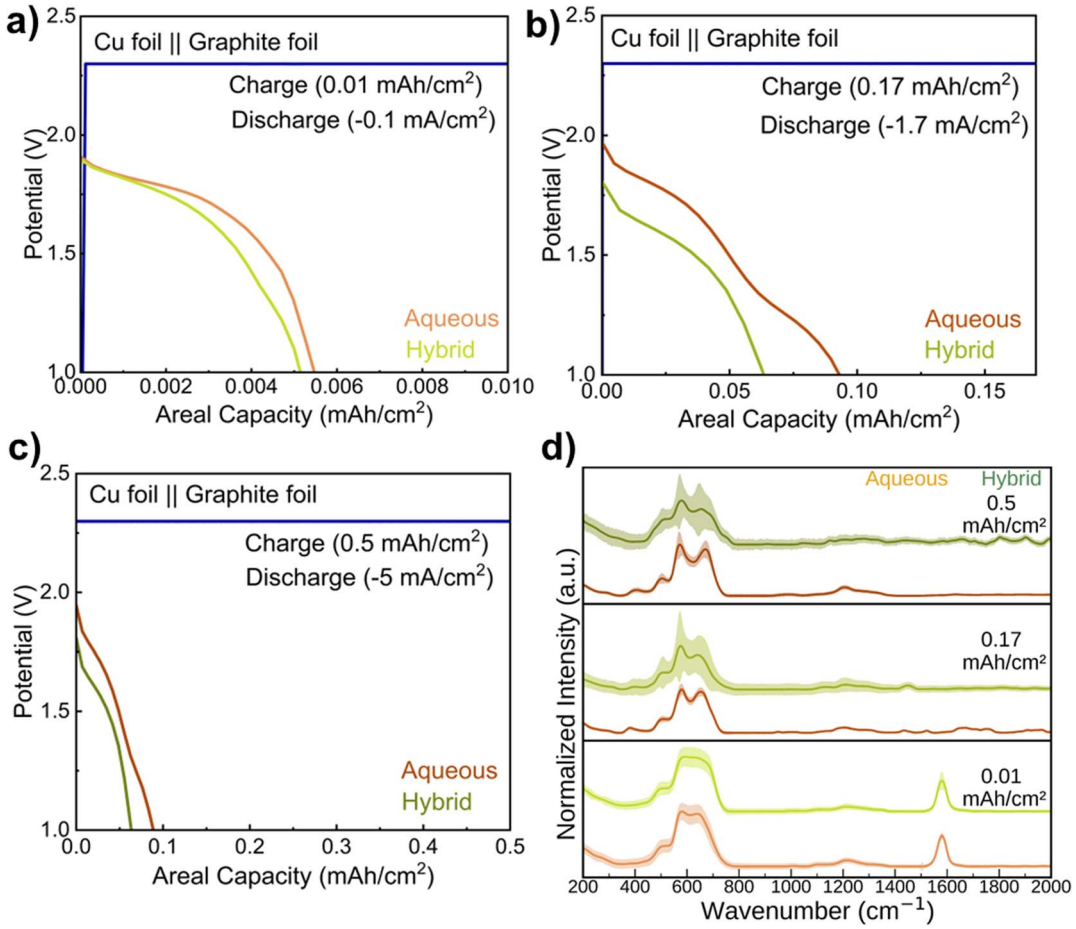

Fig. 4 Chronoamperometric deposition at 2.3 V accelerates MnO_2 growth but imposes kinetic limitations at higher areal capacities. (a–c) Galvanostatic discharge profiles after chronoamperometric deposition to capacities of 0.01, 0.17, and 0.50 mA h cm^{-2} in aqueous *vs.* hybrid electrolytes. (d) Raman spectra of MnO_2 deposited under the same conditions, showing structural evolution with increasing areal capacity.

corrosion and electrochemical side reactions, thereby preventing the pH rise that drives ZHS precipitation.

Ex situ Raman spectra of MnO_2 electrodeposited at areal capacities of 0.01, 0.17, and 0.50 mA h cm^{-2} (Fig. 4d) show the three characteristic bands of electrolytic MnO_2: ~504–510 cm^{-1}, 570–576 cm^{-1}, and 640–690 cm^{-1}; discussed for Fig. 2d. Relative to the aqueous electrolyte, the hybrid electrolyte displayed larger heterogeneity (higher standard deviation), especially for the high-wavenumber band. The high-wavenumber peaks narrowed as the areal capacity increased from 0.01 to 0.50 mA h cm^{-2}. Narrower Raman peaks signify more uniform local bonding environments and enhanced long-range structural order. Prolonged electrodeposition has been suggested to allow for structural relaxation, phase stabilization, and defect annihilation, resulting in larger, better-defined crystalline domains with reduced disorder.[43,44]

We performed SEM on the MnO_2 electrodeposited at 2.3 V (Fig. 5). Electrodeposition at 0.01, 0.17, and 0.50 mA h cm^{-2} produced a continuous MnO_2 film that thickened steadily with areal capacity in both electrolytes. In all cases, the surface remains heterogeneous consisting of a continuous film overlaid with particulate or aggregate features. Cross-sectional SEM reveals a strong dependence on electrolyte type (Fig. 5b and d & Table S4). At 0.50 mA h cm^{-2}, the MnO_2 film in the hybrid electrolyte reaches 5.22 μm. This is roughly twice the thickness observed in the aqueous electrolyte (2.62 μm). The greater thickness and denser microstructure in the hybrid case suggest higher electrodeposition efficiency and/or reduced competitive reactions during charge. A previous study using differential electrochemical mass spectrometry showed that the oxygen evolution reaction (OER) can occur during MnO_2 deposition under these conditions.[30] In the aqueous electrolyte (1 M $ZnSO_4$ + 1 M $MnSO_4$), the OER onset potential is approximately 2.1 V, whereas in the hybrid electrolyte (1 m $Zn(OTf)_2$ + 0.5 m $MnCl_2$ in 70 wt% sulfolane and 30 wt% water), the onset shifts to approximately 2.5 V. This trend agrees with our observations. Because the hybrid electrolyte exhibits a higher OER overpotential, charging at 2.3 V allows a greater fraction of the applied charge to be used for MnO_2 formation rather than OER, leading to the growth of a thicker MnO_2 film. On the other hand, a larger, more compact film may be harder to electrodissolve completely, implying sluggish solid–solid/solid–liquid interfacial processes and limited ion transport through the layer.[45,46] A thicker MnO_2 deposit behaves as a porous electrode with greater transport

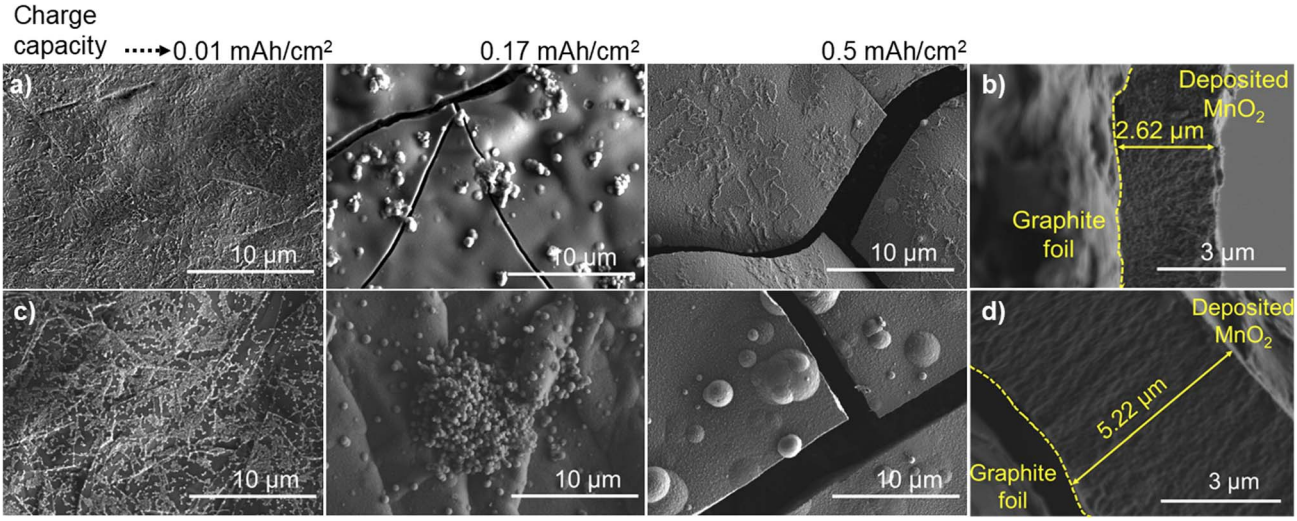

Fig. 5 Chronoamperometric deposition at 2.3 V yields denser MnO_2 layers, with morphology varying as a function of deposition thickness and electrolyte type. SEM images of MnO_2 deposited at areal capacities of 0.01, 0.17, and 0.50 mA h cm^{-2} in (a) aqueous and (c) hybrid electrolytes reveal distinct morphological changes. Cross-sectional SEM at 0.5 mA h cm^{-2} shows MnO_2 film thickness of ~2.6 µm in (b) aqueous and ~5.2 µm in (d) hybrid electrolytes.

resistance. As the film thickens, ions must move through longer and more tortuous pathways, leading to a nonuniform reaction distribution across the deposit. Under these transport-limited conditions, discharge occurs preferentially near the electrolyte-facing region, while MnO_2 in the inner part of the film remains less accessible and may not be fully utilized within the discharge cutoff potential. This transport-limited behavior is consistent with the electrochemical results (Fig. 4a–c), where the hybrid electrolyte exhibited a lower discharge capacity than the aqueous electrolyte.

We investigated the charge storage mechanism in a Swagelok cell configuration with a lower electrolyte volume (500 µL) assembled with a Cu foil anode and a high surface area graphite felt cathode (Fig. S12b) in both aqueous and hybrid electrolytes.

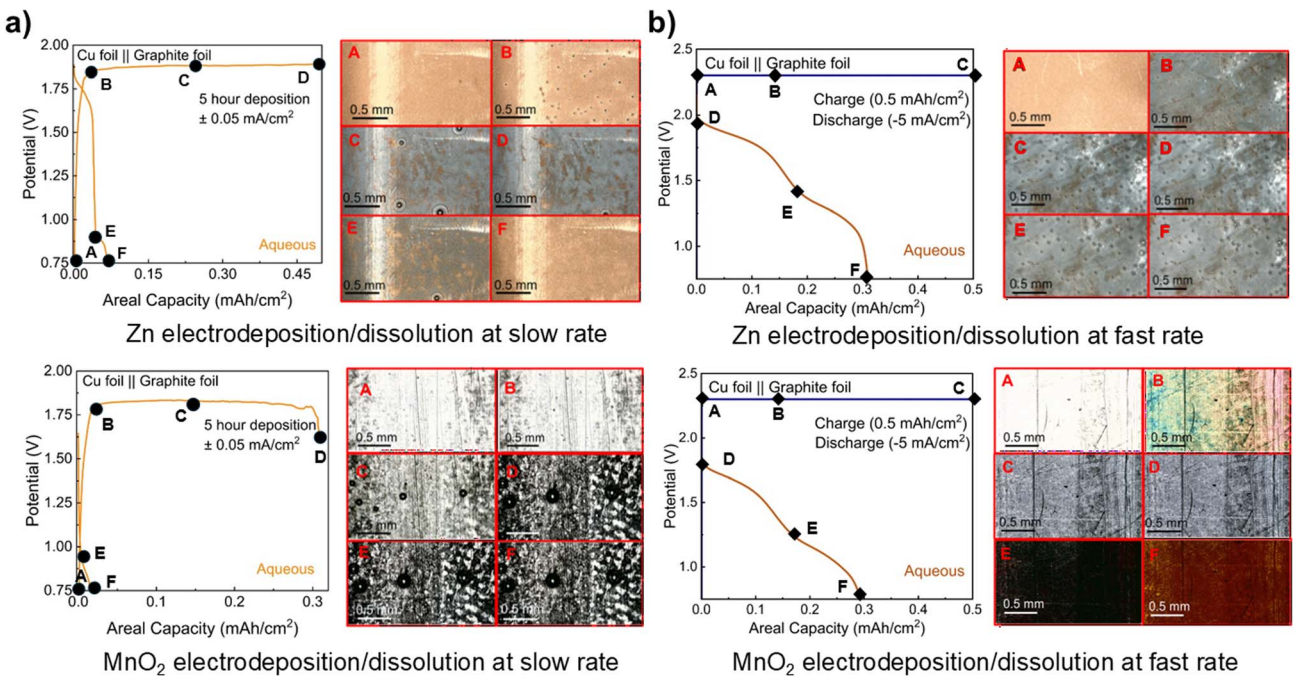

Fig. 6 *Operando* electrochemical optical microscopy reveals Zn and MnO_2 electrodeposition/dissolution dynamics during battery cycling in aqueous electrolyte. (a) Slow cycling (5 hours electrodeposition at 0.05 mA cm^{-2} followed by electrodissolution at −0.05 mA cm^{-2}) showing incomplete Zn coverage due to H_2 bubble formation and non-uniform MnO_2 growth, and low % CE. (b) Fast cycling (chronoamperometric charge at 2.3 V to 0.5 mA h cm^{-2} followed by galvanostatic discharge at −5 mA cm^{-2}) demonstrates enhanced electrodeposition during charge but incomplete electrodissolution in the aqueous electrolyte. Panels A–F are representative optical microscopy frames extracted from *in situ* video recordings.

We cycled the cells with both slow and fast charge/discharge protocols (Fig. S13–S15). For fast electrochemical protocols, we charged the cells at a constant potential of 2.3 V to reach specific areal capacities of 0.5, 1.0, 2.0, and 5.0 mA h cm^{-2}, then discharged them galvanostatically at 5, 10, 20, and 50 mA cm^{-2} (Fig. S14 & S15). The results for 0.5 mA h cm^{-2} are shown in Fig. S14a. With a porous graphite felt electrode, we found ~85% CE after charging to 0.5 mA h cm^{-2}, which is markedly higher than with planar graphite foil (CE = 17.6% in aqueous and 12.6% in hybrid electrolyte). We observed comparable discharge capacities for both aqueous and hybrid electrolytes; however, the hybrid electrolyte reveals a distinct voltage plateau near ~1.3 V.

We obtained SEM images of the electrodeposited MnO_2 at 0.5 mA h cm^{-2} (Fig. S14b–d). Plan-view SEM shows that MnO_2 fully coated the graphite felt in both electrolytes. We observed heterogeneous deposits comprising a continuous base layer with coexisting features such as ridges and aggregates distributed along the fibers. Cross-sectional SEM revealed that MnO_2 grows as conformal coatings around individual fibers in both aqueous (Fig. S14c) and hybrid electrolytes (Fig. S14d), rather than as a dense, continuous film. The deposit penetrates inward from the electrode surface to a depth of ~0.25 mm. This fiber-conformal growth increases the active surface area and shortens ion transport pathways, explaining the high % CE observed with the porous substrate. As the areal capacity increased to 1, 2, and 5 mA h cm^{-2}, the discharge capacity steadily decreased (Fig. S15). The hybrid electrolyte showed particularly poor performance at 2 and 5 mA h cm^{-2} compared to the aqueous system. We hypothesize that thicker MnO_2 deposits accumulating on the fibers create increased kinetic barriers to ion diffusion.

3.3 Real-time observation of electrodeposition/electrodissolution mechanism of Zn/MnO_2 battery

We performed *operando* electrochemical optical microscopy (EC-OM) of the Zn/MnO_2 cell to directly visualize Zn and MnO_2 electrodeposition/electrodissolution during electrochemical cycling (SI Videos 1–4). Fig. 6a provides optical frames at different points (A–F) of slow galvanostatic cycling (potential *vs.* capacity) in an aqueous electrolyte. Here, it should be noted that, during the MnO_2 optical video microscopy experiments, the laboratory temperature was relatively high, leading to partial electrolyte evaporation and a change in electrolyte concentration. This evaporation caused a decline in the charging capacity toward the end of the charging process. The optical microscopy video shows that before any Zn deposition, hydrogen bubbles nucleate on the Cu foil, impeding uniform Zn growth and leading to incomplete Zn electrodeposition. MnO_2 deposits unevenly on the graphite foil, forming patchy islands rather than a continuous film. Upon discharge, stripping halts immediately once all Zn dissolves from the Cu foil despite the presence of remaining MnO_2. It clearly indicates that the battery capacity is limited by Zn inventory. MnO_2 cannot be further utilized because there is no Zn at the anode to oxidize. This behavior is further validated by EC-OM of the hybrid electrolyte cell (Fig. 7a), where we observed dense Zn deposition without HER on Cu foil. The absence of H_2 bubbles allows more uniform Zn plating, maintaining charge balance during discharge, and allows a larger fraction of the electrodeposited MnO_2 to dissolve. This accounts for the superior discharge capacity and utilization achieved in hybrid *versus* aqueous electrolytes. Nevertheless, residual MnO_2 and Zn remain at the end of

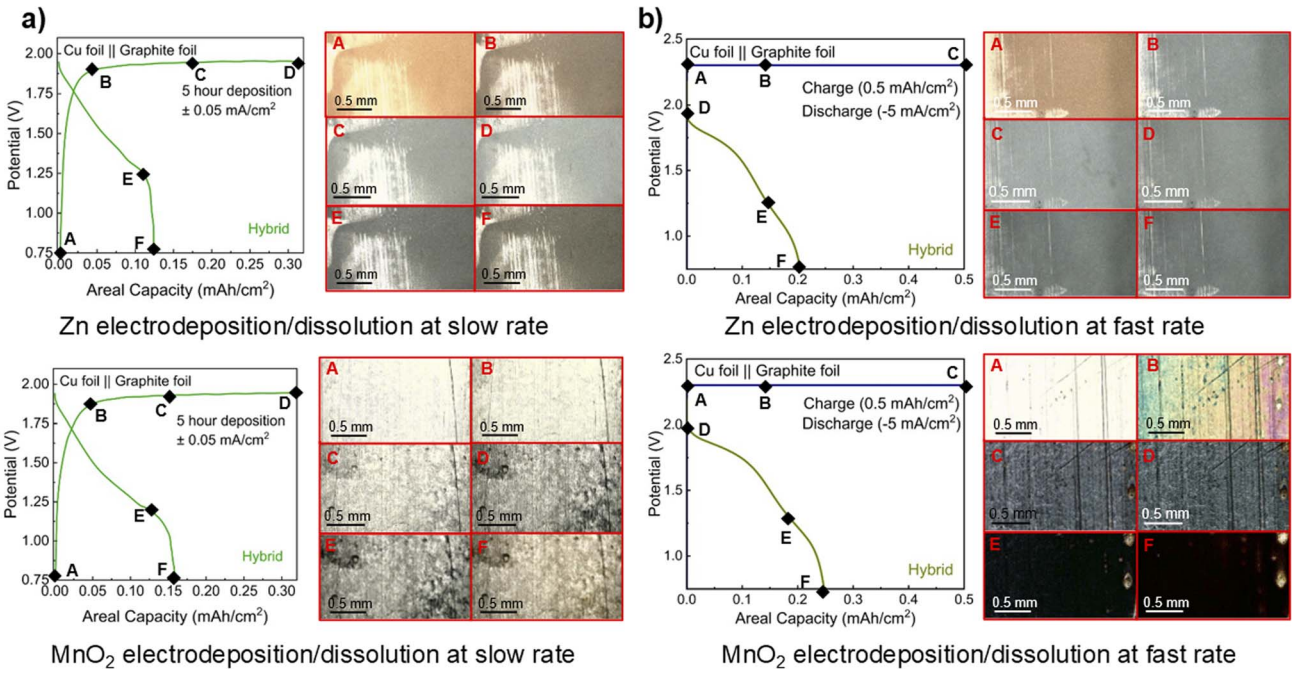

Fig. 7 Optical frames (panels A–F) from *operando* electrochemical optical microscopy reveal Zn and MnO_2 electrodeposition/dissolution dynamics during battery cycling in the hybrid electrolyte. (a) Slow cycling (5 hours electrodeposition at 0.05 mA cm^{-2} followed by electrodissolution at −0.05 mA cm^{-2}) (b) fast cycling (chronoamperometric charge at 2.3 V to 0.5 mA h cm^{-2} followed by galvanostatic discharge at −5 mA cm^{-2}).

discharge, implying incomplete stripping within the chosen potential window. To achieve ~100% utilization would require extending the window to a lower cutoff potential.

Fig. 6b presents *operando* optical frames (A–F) captured during fast cycling: charging to 0.50 mA h cm^{-2} at 2.3 V, then discharging at a 5 mA cm^{-2} to 0.75 V in the aqueous electrolyte. High overpotentials drive more extensive Zn deposition than under slow cycling, yet vigorous H_2 bubble evolution continues throughout the charging. The MnO_2 electrodeposits as a uniform thin film, and the electrode surface changes in color as the thickness grows, reflecting continuous film formation in the early stages. Upon discharge, the film turns brown as MnO_2 electrodissolves, but both Zn and residual MnO_2 persist at the end of discharge providing evidence of incomplete stripping within the applied potential window. These results underscore the kinetic and transport limitations of thick MnO_2 films at the cathode that prevent full material removal during rapid discharge. Under high overpotential charging, Zn electrodeposition becomes non-uniform and can be dendritic; portions of the deposit may become poorly connected or electrically isolated ("dead Zn") and therefore cannot be fully accessed during subsequent electrodissolution.[47] In the hybrid electrolyte (Fig. 7b), the same phenomena occur during MnO_2 electrodeposition and electrodissolution at fast charge–discharge: most of the MnO_2 deposited during charge remains on the cathode upon discharge, highlighting persistent constraints on rapid cycling reversibility. On the other hand, we observe no HER bubbles on the Cu foil during Zn deposition.

4. Conclusions

This work reports how electrochemical protocols and electrolyte composition govern the mechanisms of Zn/MnO_2 electrodeposition and electrodissolution in an initially "anode-/cathode-free" battery configuration. In mildly acidic aqueous Zn/MnO_2 systems, three-electrode cell cycling achieved 88% CE, whereas two-electrode cells delivered only 12%, highlighting how cell configuration and anode side reactions influence the overall battery efficiency and capacity. Electrochemical cycling using different charge–discharge protocols revealed a clear trend among discharge capacity, deposition time, and deposited areal capacity in both aqueous and hybrid electrolytes. Under slow galvanostatic cycling, the hybrid electrolyte delivers higher discharge capacity than the aqueous system, whereas in fast charge/discharge, the trend reverses, with the hybrid electrolyte exhibiting lower % CE. SEM images show that slow cycling produces a uniform, homogeneous MnO_2 film that grows steadily over time, while fast charging at a constant potential yields a thick, heterogeneous film in a short deposition period. During fast charging at 2.3 V, hybrid electrolytes electrodeposit roughly twice as much MnO_2 as aqueous electrolytes due to the suppression of HER and OER. Structural heterogeneity of electrodeposited MnO_2 is revealed by *ex situ* Raman spectroscopy. The structural heterogeneity arises from the electrodeposition of mixed gamma (γ) and epsilon (ε) MnO_2 phases, which are defect or disordered phases characteristic of electrolytic MnO_2. This heterogeneity decreases with longer deposition times during slow cycling but increases under fast cycling, correlating the thicker, more disordered films seen in SEM.

Electrodeposition/electrodissolution dynamics of Zn/MnO_2 were revealed by *operando* EC-OM. During slow cycling in the aqueous electrolyte, anode-side HER restricts Zn deposition, inducing a Zn-limited discharge, lowering the discharge capacity of the battery system. Switching to a hybrid electrolyte suppresses HER, enables more complete Zn deposition, and thereby increases MnO_2 dissolution and overall discharge capacity. Fast charging drives a rapid buildup of thick Zn and MnO_2 layers, but MnO_2 stripping slows due to kinetic limitation. Although hybrid electrolytes further increase Zn and MnO_2 electrodeposition by suppressing side reactions like HER and OER, they also heighten the kinetic limitations during electrodissolution, reducing utilization under fast charge–discharge cycling. Using porous graphite felt substrates mitigates this issue: MnO_2 grows conformally in thinner layers on individual fibers, improving the % CE. These results underscore that stabilization of the zinc anode and the design of porous conductive scaffolds at the cathode are essential to maximize Zn/MnO_2 battery performance for LDES.

Conflicts of interest

There are no conflicts to declare.

Data availability

Data from this work is openly available at https://doi.org/10.5281/zenodo.17833888.

Supplementary information (SI): schematics of electrochemical cells, results of galvanostatic and chronoamperometric experiments, and SEM images of the porous graphite felt substrate. See DOI: https://doi.org/10.1039/d6ta00154h.

Acknowledgements

We thank Jinghan Li, Prof. Linda Nazar, and Prof. Véronique Balland for valuable discussions and the Aqueous Battery Consortium for inspiring this work. This work was supported by the Jake and Jennifer Hooks Distinguished Professorship and the Goodnight Early Career Innovator grant at NC State University. Research by C. K. was supported by the NC State College of Engineering Enhancement Fee. This work was performed in part at the Analytical Instrumentation Facility (AIF) at North Carolina State University, which is supported by the State of North Carolina and the National Science Foundation (award number ECCS-2025064). The AIF is a member of the North Carolina Research Triangle Nanotechnology Network (RTNN), a site in the National Nanotechnology Coordinated Infrastructure (NNCI). The Authors used a generative AI chatbot (OpenAI ChatGPT) to write the Python scripts for synchronizing electrochemical datasets with optical microscopy videos and refine the language and grammar of this manuscript. After using this tool, the Authors reviewed and edited the contents and take full responsibility for the final content of the manuscript.

References

1 J. Twitchell, K. DeSomber and D. Bhatnagar, *J. Energy Storage*, 2023, **60**, 105787.
2 N. A. Sepulveda, J. D. Jenkins, A. Edington, D. S. Mallapragada and R. K. Lester, *Nat. Energy*, 2021, **6**, 506–516.
3 Why Long-Duration Energy Storage Matters | ARPA-E, https://arpa-e.energy.gov/news-and-events/news-and-insights/why-long-duration-energy-storage-matters, (accessed November 27, 2025).
4 P. Albertus, J. S. Manser and S. Litzelman, *Joule*, 2020, **4**, 21–32.
5 M. Dixit, B. Witherspoon, N. Muralidharan, M. M. Mench, C.-B. M. Kweon, Y.-K. Sun and I. Belharouak, *ACS Energy Lett.*, 2024, **9**, 3780–3789.
6 G. P. Wheeler, L. Wang and A. C. Marschilok, *Beyond Li-Ion Batteries for Grid-Scale Energy Storage*, Cambridge University Press, Cambridge, 2022.
7 P. Denholm, W. Cole and N. Blair, *Moving beyond 4-Hour Li-Ion Batteries: Challenges and Opportunities for Long(er)-Duration Energy Storage*, National Renewable Energy Laboratory (NREL), Golden, CO (United States), 2023.
8 C. Xu, B. Li, H. Du and F. Kang, *Angew. Chem., Int. Ed.*, 2012, **51**, 933–935.
9 T. Shoji and T. Yamamoto, *J. Electroanal. Chem.*, 1993, **362**, 153–157.
10 E. D. Spoerke, H. Passell, G. Cowles, T. N. Lambert, G. G. Yadav, J. Huang, S. Banerjee and B. Chalamala, *MRS Energy Sustain.*, 2022, **9**, 13–18.
11 G. Li, W. Chen, H. Zhang, Y. Gong, F. Shi, J. Wang, R. Zhang, G. Chen, Y. Jin, T. Wu, Z. Tang and Y. Cui, *Adv. Energy Mater.*, 2020, **10**, 1902085.
12 M. Chamoun, W. R. Brant, C.-W. Tai, G. Karlsson and D. Noréus, *Energy Storage Mater.*, 2018, **15**, 351–360.
13 I. Aguilar, P. Lemaire, N. Ayouni, E. Bendadesse, A. V. Morozov, O. Sel, V. Balland, B. Limoges, A. M. Abakumov, E. Raymundo-Piñero, A. Slodczyk, A. Canizarès, D. Larcher and J.-M. Tarascon, *Energy Storage Mater.*, 2022, **53**, 238–253.
14 H. Pan, Y. Shao, P. Yan, Y. Cheng, K. S. Han, Z. Nie, C. Wang, J. Yang, X. Li, P. Bhattacharya, K. T. Mueller and J. Liu, *Nat. Energy*, 2016, **1**, 16039.
15 A. Singh, L. Ouassi, K. Allemang, J.-F. Lemineur, O. Sel, F. Kanoufi and C. Laberty-Robert, *J. Power Sources*, 2025, **625**, 235585.
16 Y. Li, X. Zheng, E. Z. Carlson, X. Xiao, X. Chi, Y. Cui, L. C. Greenburg, G. Zhang, E. Zhang, C. Liu, Y. Yang, M. S. Kim, G. Feng, P. Zhang, H. Su, X. Guan, J. Zhou, Y. Wu, Z. Xue, W. Li, M. Bajdich and Y. Cui, *Nat. Energy*, 2024, **9**, 1350–1359.
17 T. N. T. Tran, S. Jin, M. Cuisinier, B. D. Adams and D. G. Ivey, *Sci. Rep.*, 2021, **11**, 20777.
18 S. Han, S. Park, S.-H. Yi, W. B. Im and S.-E. Chun, *J. Alloys Compd.*, 2020, **831**, 154838.
19 W. Huang, J. Li and Y. Xu, *Materials*, 2017, **10**, 1205.
20 A. Rana, S. Paul, A. Bhadouria, A. Bano, J. H. Nguyen, Md. A. Faisal, K. Roy, B. M. Tackett and J. E. Dick, *Adv. Energy Mater.*, 2025, **15**, e03155.
21 C. F. Bischoff, O. S. Fitz, J. Burns, M. Bauer, H. Gentischer, K. P. Birke, H.-M. Henning and D. Biro, *J. Electrochem. Soc.*, 2020, **167**, 020545.
22 G. Lai, Z. Zhao, H. Zhang, X. Hu, B. Lu, S. Liang and J. Zhou, *Nat. Commun.*, 2025, **16**, 2194.
23 X. Zeng, K. Xie, S. Liu, S. Zhang, J. Hao, J. Liu, W. K. Pang, J. Liu, P. Rao, Q. Wang, J. Mao and Z. Guo, *Energy Environ. Sci.*, 2021, **14**, 5947–5957.
24 L. Cao, D. Li, T. Pollard, T. Deng, B. Zhang, C. Yang, L. Chen, J. Vatamanu, E. Hu, M. J. Hourwitz, L. Ma, M. Ding, Q. Li, S. Hou, K. Gaskell, J. T. Fourkas, X.-Q. Yang, K. Xu, O. Borodin and C. Wang, *Nat. Nanotechnol.*, 2021, **16**, 902–910.
25 I. Aguilar, J. Brown, L. Godeffroy, F. Dorchies, V. Balland, F. Kanoufi and J.-M. Tarascon, *Joule*, 2025, **9**, 101784.
26 H. Li, S. Wang, Z. Feng, Z. Liu, Y. Liu, M. Yang, P. Gao, L. Fu and X. Zhao, *Adv. Mater.*, 2025, **37**, e14328.
27 C. Li, R. Kingsbury, A. S. Thind, A. Shyamsunder, T. T. Fister, R. F. Klie, K. A. Persson and L. F. Nazar, *Nat. Commun.*, 2023, **14**, 3067.
28 H. Lyu, J. T. Kim, D. Cheng, X. Yuan, M. Anderson, K. Liang, J. Yu, P. Sautet, R. Kaner and Y. Li, *ACS Energy Lett.*, 2025, **10**, 2924–2933.
29 Y. Wang, T. Wang, S. Bu, J. Zhu, Y. Wang, R. Zhang, H. Hong, W. Zhang, J. Fan and C. Zhi, *Nat. Commun.*, 2023, **14**, 1828.
30 J. Li, C. Li, B. Liu, Y. Li, O. Borodin and L. F. Nazar, *Nat. Energy*, 2026, **11**, 299–312.
31 M. Li, Z. Li, X. Wang, J. Meng, X. Liu, B. Wu, C. Han and L. Mai, *Energy Environ. Sci.*, 2021, **14**, 3796–3839.
32 H. Qiu, X. Du, J. Zhao, Y. Wang, J. Ju, Z. Chen, Z. Hu, D. Yan, X. Zhou and G. Cui, *Nat. Commun.*, 2019, **10**, 5374.
33 Y. Deng, H. Wang, M. Fan, B. Zhan, L.-J. Zuo, C. Chen and L. Yan, *J. Am. Chem. Soc.*, 2023, **145**, 20109–20120.
34 J. Yang, J. Cao, Y. Peng, W. Yang, S. Barg, Z. Liu, I. A. Kinloch, M. A. Bissett and R. A. W. Dryfe, *ChemSusChem*, 2020, **13**, 4103–4110.
35 I. Stoševski, A. Bonakdarpour, B. Fang, P. Lo and D. P. Wilkinson, *Electrochim. Acta*, 2021, **390**, 138852.
36 J. E. Post, D. A. McKeown and P. J. Heaney, *Am. Mineral.*, 2021, **106**, 351–366.
37 C. Julien, M. Massot, S. Rangan, M. Lemal and D. Guyomard, *J. Raman Spectrosc.*, 2002, **33**, 223–228.
38 C.-H. Kim, Z. Akase, L. Zhang, A. H. Heuer, A. E. Newman and P. J. Hughes, *J. Solid State Chem.*, 2006, **179**, 753–774.
39 H. Yang, Y. Yang, W. Yang, G. Wu and R. Zhu, *Energy Environ. Sci.*, 2024, **17**, 1975–1983.
40 A. Rana, S. Paul, A. Bhadouria, J. H. Nguyen, J. F. Koons, C. Li, A. Das, K. Roy, B. M. Tackett and J. E. Dick, *Joule*, 2025, **9**, 102167.
41 M. Mateos, N. Makivic, Y.-S. Kim, B. Limoges and V. Balland, *Adv. Energy Mater.*, 2020, **10**, 2000332.
42 L. Godeffroy, I. Aguilar, J. Médard, D. Larcher, J.-M. Tarascon and F. Kanoufi, *Adv. Energy Mater.*, 2022, **12**, 2200722.

43 D. Tuschel, Peak Shape and Closely Spaced Peak Convolution in Raman Spectra | Spectroscopy Online, https://www.spectroscopyonline.com/view/peak-shape-and-closely-spaced-peak-convolution-in-raman-spectra, (accessed November 27, 2025).
44 S. V. Koniakhin, O. I. Utesov and A. G. Yashenkin, *Diamond Relat. Mater.*, 2024, **146**, 111182.
45 J. Newman and W. Tiedemann, *AIChE J.*, 1975, **21**, 25–41.
46 J. S. Dunning, D. N. Bennion and J. Newman, *J. Electrochem. Soc.*, 1973, **120**, 906.
47 V. Yufit, F. Tariq, D. S. Eastwood, M. Biton, B. Wu, P. D. Lee and N. P. Brandon, *Joule*, 2019, **3**, 485–502.